Tracking based, high-resolution single-shot multimodal x-ray imaging in the laboratory enabled by the sub-pixel resolution capabilities of the MÖNCH detector

E. S. Dreier, A. Bergamaschi, G. K. Kallon, R. Brönnimann, U. L. Olsen, A. Olivo, and M. Endrizzi

View Online   Export Citation   CrossMark

ARTICLES YOU MAY BE INTERESTED IN

Tracking based, high-resolution single-shot multimodal x-ray imaging in the laboratory enabled by the sub-pixel resolution capabilities of the MÖNCH detector

E. S. Dreier,[1,a] (iD) A. Bergamaschi,[2] (iD) G. K. Kallon,[3] (iD) R. Brönnimann,[4] U. L. Olsen,[5] (iD) A. Olivo,[3] (iD)
and M. Endrizzi[3] (iD)

AFFILIATIONS

[1]Niels Bohr Institute, University of Copenhagen, Universitetsparken 5, 2100 København Ø, Denmark
[2]Photon Science Division, Paul Scherrer Institut, Forschungsstrasse 111, 5232 Villigen PSI, Switzerland
[3]UCL Department of Medical Physics and Biomedical Engineering, Malet Place, Gower Street, London WC1E BT, United Kingdom
[4]EMPA, Swiss Federal Laboratories for Materials Science and Technology, Überlandstrasse 129, 8600 Dübendorf, Switzerland
[5]Department of Physics, Technical University of Denmark, Anker Engelundsvej 1, 2800 Kgs Lyngby, Denmark

[a]Author to whom correspondence should be addressed: erik.dreier@food.ku.dk

ABSTRACT

The simultaneous retrieval of x-ray attenuation, phase, and scattering using multimodal imaging techniques is finding increasing use in a range of applications, from medicine to materials science. Most techniques rely on the mechanical movement of an optical element (e.g., a grating or a mask) to obtain the multimodal images. While single-shot approaches exist, they typically employ detector pixels smaller than the grating period, often with low detection efficiency, and are limited in resolution unless either the sample or the optical element is displaced in various positions and multiple frames are collected. In this paper, we replace mechanical motion with the MÖNCH detector's capability to reach sub-pixel resolutions by interpolating between neighboring pixels collecting the charge generated by a single x-ray event. This enabled us to obtain the pilot demonstration of a laboratory-based high-resolution, single-shot multimodal imaging technique capable of simultaneously retrieving attenuation, directional differential phase, and scatter images, without any mechanical movement. We show that our proof-of-concept setup enables a single-shot resolution of 19.5 μm and that the resulting images provide sufficient information to produce a reliable sample thickness map. Furthermore, we demonstrate that the setup is capable of producing single-shot directional scattering images, while leaving open the option to further increase the resolution by using sample dithering.

Published under license by AIP Publishing. https://doi.org/10.1063/5.0027763

Following early demonstration that x-ray dark field images could be acquired with a laboratory source,[1] a dark field (or ultra-small angle scatter, USAXS) was integrated with phase and attenuation contrast,[2] which is sometimes referred to as multimodal x-ray imaging. Multimodal imaging has since grown significantly, showing potential for lung imaging[3] (including in human sized samples[4,5]) and breast calcifications[6,7] in medicine and applications as diverse as barley sprouting[8] and microcrack detection[9] in materials science. Directional scatter imaging implementations have been developed, which can detect the orientation of fibers smaller than the image resolution,[10] and phase tomography has been shown to provide volumetric reconstruction with increased sensitivity for light materials.[11,12]

To date, several lab-based approaches capable of multimodal imaging have been developed,[6,13–17] among which is edge illumination.[6,13] The double mask edge-illumination setup uses a pre-sample mask with a regular series of apertures to split the beam generated by an incoherent source into a plurality of beamlets. A second mask is placed in contact with the detector, with every aperture aligned with the center of a pixel. The sample mask is slightly offset with respect to the detector mask, in such a way that each beamlet straddles the edge of an aperture in the latter. Refraction induced by a sample placed immediately downstream of the sample mask then varies the amount of each beamlet captured by the apertures in the detector mask, thus translating a phase-related change such as refraction into an intensity

difference. A simplification is offered by the beam-tracking approach,[14] where the detector mask is eliminated, and sample-induced changes in the beamlets' position and width are analyzed directly by using a detector with pixels significantly smaller than the mask aperture pitch. This enables single-shot retrieval of multimodal images with limited requirements on beam coherence and setup alignment, albeit at a resolution equal to the mask period. Beam tracking with 2D sensitivity was demonstrated using single photon localization with a Timepix3 detector,[18] making it possible to simultaneously measure directional scattering and differential phase.[19] However, this required a skipped mask, i.e., a mask with an aperture pitch at least as large as two pixels when projected onto the detector, limiting the resolution. Without sample "dithering" (the recombination of multiple frames acquired while the sample displaced at different positions), single-shot bi-directional retrieval of scattering and differential phases has only been shown with a spatial resolution of 150 μm. Now, we demonstrate a beam-tracking setup capable of single-shot retrieval of attenuation, bi-directional differential phase, and scatter images with a spatial resolution of 19.5 μm using a non-skipped mask. With a higher resolution, this also allows for a more efficient use of the x-ray source, as it increases the mask open fraction compared to the skipped mask case.

It should be noted that single-shot approaches are possible and have indeed been implemented, with scintillator-based solutions.[15,20–23] However, in that case, the pixel size needs to be smaller than the period of the optical element (e.g., mask or grating) being used. In indirect conversion detectors, the need for small pixels often implies the use of thin scintillators to limit the lateral spread of the visible light photons, which has a reverse effect on detective quantum efficiency.

Our beam tracking method was enabled by the analogue readout, direct converting MÖNCH detector combined with a small pitch tungsten mask. MÖNCH is a charge integrating, hybrid pixel detector with a pixel size of 25 μm. The current prototype features 400 × 400 pixels (1 × 1 cm^2), which can be read out at a maximum frame rate of 1.5 kHz.[24] MÖNCH exploits the charge sharing effect to achieve a spatial resolution of a few μm, by interpolating between neighboring pixels collecting the charge generated by single photons.[25]

The experimental setup is shown in Fig. 1. It features a Hamamatsu L12161–07 source operated at 40 kV and 10 W, at which the nominal focal spot is <7 μm. The mask consists of an array of conically shaped apertures with a pitch of 16.7 μm, created by laser ablation into a 100-μm-thick tungsten foil. The laser ablation process means that the size of the apertures is somewhat irregular, averaging approximately 5 μm when measured on the laser's exit side. The mask was placed at Z_{XM} = 675 mm from the source, ultimately resulting in a partially overlapping array of beamlets with a Full Width Half Maximum (FWHM) at the sample of 15 ± 2 μm, calculated by back-projecting the measured beamlet FWHM at the detector of 19 ± 2 μm. The mask-to-detector (Z_{MD} = 335 mm) and sample-to-detector (Z_{SD} = 220 mm) distances were adjusted so that the beamlet pitch at the detector equals that of the pixel, i.e., 25 μm. This led to a distance between the beamlets at the sample of 19.5 μm, which defines the single-shot resolution.

The center-of-mass calculation of the charge distribution shared among adjacent pixels[25,26] allowed single photon localization with a significantly higher resolution than the physical pixel size, making it possible to resolve the beamlets. This overcomes the resolution/
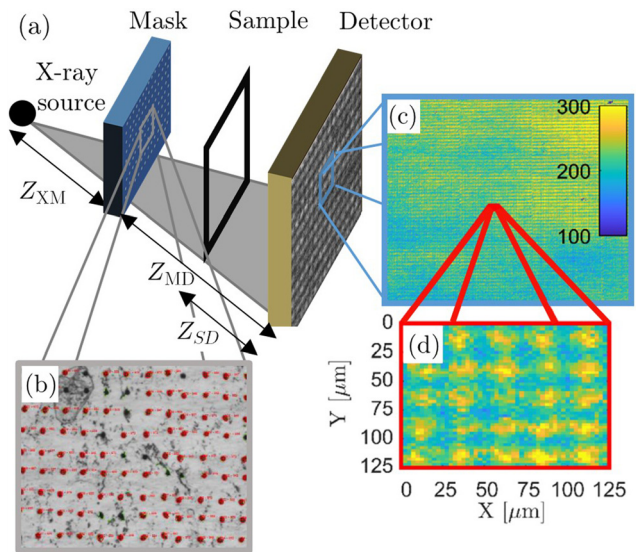
FIG. 1. Schematic of the experimental setup, consisting of a micro-focal source, pre-sample mask, and MÖNCH detector (a). The mask has a periodic array of holes with an average pitch of 16.7 μm (b). Using single photon localization and η-distribution correction, the beamlets are resolved with a virtual pixel size of 2.5 μm (c), highlighted with zoom-in in panel (d). The color bar in panel (c) expresses the detected number of counts.

detection efficiency compromise required by, e.g., indirect conversion detectors. In our case, the efficiency is determined by x-ray absorption in the 320-μm-thick silicon sensor,[27] and it can be further increased by switching to higher Z materials. The analogue readout also allows for a measurement of the photon energy with a resolution mainly limited by the electronic noise (∼1 keV FWHM for a 2 × 2 pixel cluster[28]). A high frame rate is required to isolate single photons, determine their energy, and apply the interpolation algorithm: we used a frame rate of 1 kHz, which allows the detection of a maximum flux of about 5000 photons mm^{-2} s^{-1}. For the purpose of resolving the beamlets, the photons' sub-pixel position was binned into virtual pixels of 2.5 μm, obtained by subdividing the physical pixel into 10 × 10 bins when applying the interpolation algorithm. This is comparable with the effective spatial resolution of 2–5 μm of the detector, which depends on the photon energy, the detector operating parameters, and the absorption position of the photon within the pixel (lowest in the center due to the absence of charge sharing).[25] An energy-dependent interpolation algorithm was applied to account for the non-uniform charge sharing within the pixel[25] and is briefly described in the supplementary material. To obtain sufficient photon count statistics at a resolution of 2.5 μm, the acquisition time was for all experiments set to 1000 s, per sample position. The energy resolving capability of the detector was exploited to select photons in the range of 5–25 keV in order to remove the background given by high-energy photons transmitted through the mask and low-energy electronic noise.

Attenuation, differential phase, and scattering images can be retrieved with our setup by measuring the sample introduced distortions to the beamlets. Upon passing through a sample, a fraction t of the initial beamlet intensity distribution $i_0(\theta_x, \theta_y)$ will be transmitted,

depending on the sample thickness and attenuation coefficient μ; the beamlet's center of gravity will be refracted by $\Delta\theta_x$ and $\Delta\theta_y$ transverse to the propagation direction by local sample density gradients and its shape broadened by the sample scattering function $s(\theta_x, \theta_y)$. The result can be described as a convolution,[14]

$$i(\theta_x, \theta_y) = t\left[i_0(\theta_x - \Delta\theta_x, \theta_y - \Delta\theta_y) * s(\theta_x, \theta_y)\right]. \quad (1)$$

Note that $i_0(\theta_x, \theta_y)$ itself can be described as a convolution of mask aperture, detector point spread function, and projected source size.[14] The beamlet shape can be quantified through its moments;[29] along the x-direction, these are defined as

$$m = 0 \quad M^0 = \sum_n^N i(n), \quad (2)$$

$$m = 1 \quad M_x^1 = \sum_n^N \frac{i(n)x(n)}{M^0}, \quad (3)$$

$$m = 2 \quad M_x^2 = \sum_n^N \frac{i(n)(x(n) - M_x^1)^2}{M^0}. \quad (4)$$

In all the above cases, the sum is taken over the intensity of the N virtual sub-pixels n illuminated by the beamlet. Similarly, the moments can be calculated for the y direction and in the absence of the sample. Assuming a perfectly absorbing mask, moments with (M^m) and without (M_0^m) the sample can be used to retrieve the directional differential phase, $\Delta\theta_x = \sin^{-1}\frac{M_x^1 - M_{x,0}^1}{z_{SD}}$ and $\Delta\theta_y = \sin^{-1}\frac{M_y^1 - M_{y,0}^1}{z_{SD}}$, and attenuation $A = \log\left(\frac{M^0}{M_0^0}\right)$. The second order moment is the variance of the beamlet's intensity distribution,[18] with $\sigma_{x,y}^2 = M_{x,y}^2$.

A rigorous, quantitative separation of material characteristics, such as μ and the unit decrement of the refractive index δ, from the sample thickness would require a full CT acquisition, which was made impossible by the time constraints imposed on our experiment. However, a single material assumption still allows retrieving the sample thickness by integrating the refraction angle along x and y, e.g., through the Fourier differentiation theorem,[21]

$$T = \frac{1}{\delta} F^{-1}\left[\frac{F(\Delta\theta_x + i\Delta\theta_y)}{ik_x - k_y}\right], \quad (5)$$

where (k_x, k_y) are the spatial frequencies in Fourier space. Importantly, an independent estimation of the thickness can be obtained from the attenuation image using Beer–Lambert's law (again assuming a single material), which provides a means to test the reliability of the retrieved thicknesses.

Directional scattering images are obtained through the directional variance (second order moments) and the covariance,[18]

$$\sigma_{xy} = \frac{\left(\sum_n^N (x(n) - M_x^1)(y(n) - M_y^1)i(n)\right)}{M^0}. \quad (6)$$

The beamlet intensity distribution at the detector without a sample is found to be well described by a Gaussian function. Assuming that the scattering function is also Gaussian[14,30] and, therefore, that $i_0(\theta_x, \theta_y)$ and $s(\theta_x, \theta_y)$ can be represented by multivariate normal distribution

with co-variance matrices Σ_{i_0} and Σ_i, the scattering function can be obtained from

$$\Sigma_s = \Sigma_i - \Sigma_{i_0} = \begin{pmatrix} \Delta\sigma_x^2 & \Delta\sigma_{xy} \\ \Delta\sigma_{xy} & \Delta\sigma_y^2 \end{pmatrix}, \quad (7)$$

where $\Delta\sigma_x^2$, $\Delta\sigma_y^2$, and $\Delta\sigma_{xy}$ are the differences in variance and covariance with and without a sample in the beam. The magnitude and orientation of the scattering function $s(\theta_x, \theta_y)$ are given by the eigenvalue and eigenvector of the covariance matrix Σ_s.

The preliminary nature of this experiment meant that some aspects were not fully optimized; in particular, we had a significant overlap between neighboring beamlets, a background signal probably due to scattering from the sample container, and relatively low counting statistics due to the use of a low-power x-ray source. This made thickness retrieval somewhat less accurate and meant that data needed to be averaged and backgrounds carefully subtracted to enable the retrieval of quantitatively exact values. An example of these procedures and their application to a plastic phantom are reported in the supplementary material (Fig. S3). However, the method's ability to retrieve a similar thickness using independent approaches based on phase and attenuation provides an indication of its reliability. Figure 2 shows that, under the single material assumption, the method can retrieve the sample thickness in a single shot; Fig. 3 then shows that thicknesses retrieved using independent methods are to a good approximation comparable.

Figures 2(a) and 2(c) show thickness maps obtained from attenuation and differential phase images retrieved from a dithered acquisition in which 25 frames were acquired, while the sample was displaced in a 5×5 grid with x and y steps equivalent to 1/5 of the mask period and recombined into an image with an effective pixel size of 3.9 μm. Figure 2(e) shows the thickness map obtained from the differential phase image retrieved from a single-shot dataset (effective pixel size 19.5 μm). Figures 2(b), 2(d), and 2(f) show zoomed-up regions of the same images. Finally, for completeness, Figs. 2(g) and 2(h) show the (dithered) horizontal and vertical differential phase images of the same enlarged image.

The thickness was calculated assuming a dry beetle with a homogeneous density of $\rho = 0.21$ g cm^{-3}. The dry density of insects is almost constant with $\rho = [0.20, 0.23]$ g cm^{-3}, slightly increasing as a function of insect size according to the relationship between the volume and the dry mass $\log(V) = 1.019 \log(m) + 1.46$ reported in Ref. 31. The composition of the beetle was assumed to be the protein-dominated composition approximated with the generic formula of α-amino acid (H2N-CHR-COOH), disregarding the organic side chain R. Values of δ and of the attenuation coefficient μ were obtained assuming an x-ray energy of $E = 10.5$ keV, equal to the weighted average energy of the x-ray beamlets measured at the detector within the selected photon energy range of 5–25 keV. The mean weighted x-ray energy is calculated based on a reference 40 kV tungsten source spectrum, attenuated by a 2000 μm beetle sample, measured with the detector's sensitivity estimated from the expected photo-electric absorption in a 320 μm silicon sensor.

We note that, although the relatively low energy used in this experiment adds to its preliminary nature, it also means that attenuation images are dominated by the photoelectric absorption with very little contribution from Compton scattering, which makes our
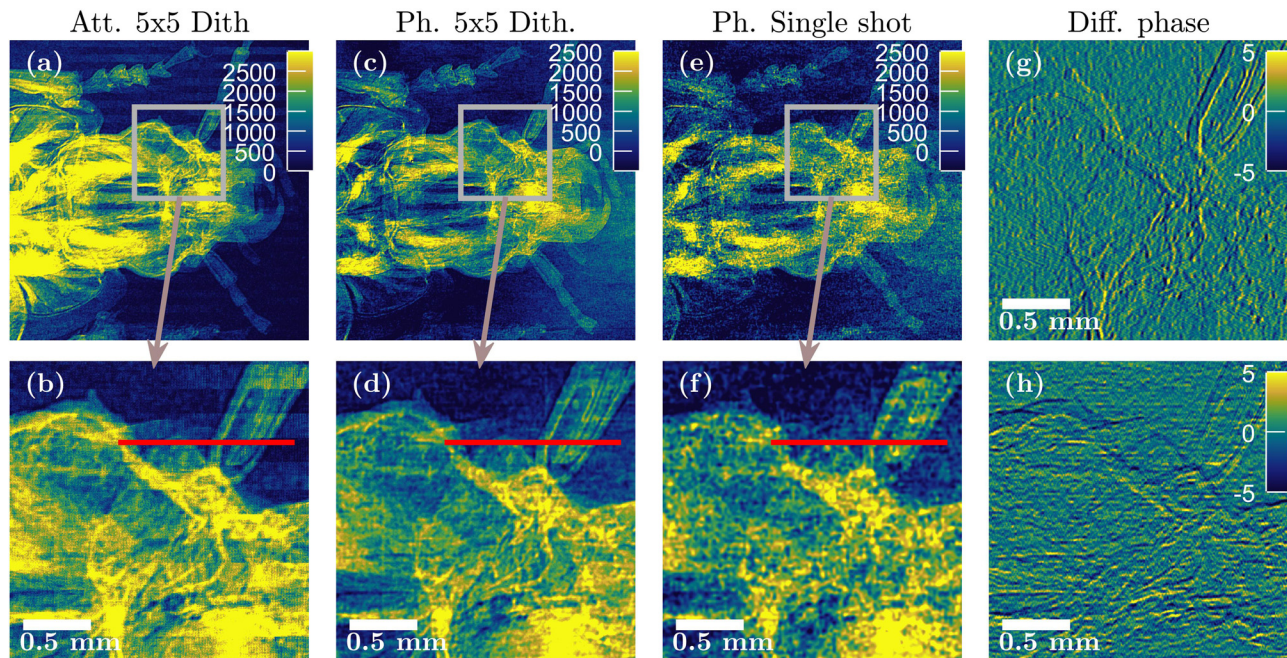
FIG. 2. Thickness maps of a beetle retrieved from the dithered attenuation image (a), dithered differential phase image (c), and single-shot differential phase image (e); all color scales in μm. Panels (b), (d), and (f) right underneath show zoomed-in regions from the region-of-interest highlighted in panels (a), (c), and (e). Panels (g) and (h) show the horizontal and vertical differential phase images of the zoomed-in region; color scales in μrad.

assumption of independence between phase and attenuation-based thickness measurements even more robust.

A constant was added to thickness maps retrieved from differential phase images to obtain a zero-average background; this was made necessary by field-of-view limitations, making it impossible to extend integration over the full object. Profiles corresponding to the red line indicated in panels (b), (d), and (f) are shown in Fig. 3.
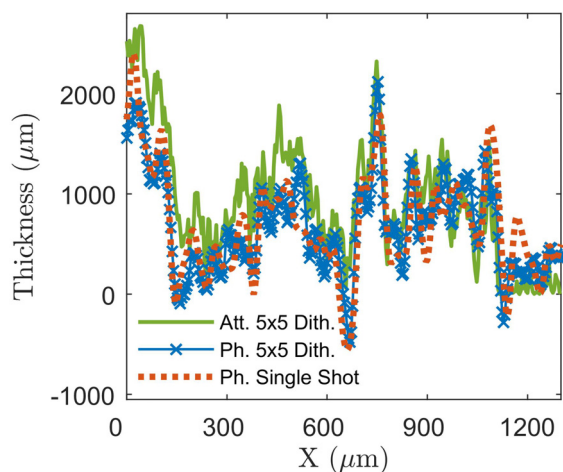
FIG. 3. Thickness profile corresponding to the red line in panels (b), (d), and (f) of Fig. 2. The single-shot phase profile has been interpolated to appear with the same number of points as the dithered phase profile.

Profiles in Fig. 3 show that thickness values retrieved from attenuation and phase images are to a reasonable approximation in qualitative agreement, confirming their reliability. Furthermore, the fact that (resolution aside) the single-shot method yields approximately the same result demonstrates that the method's reliability is not affected by single-shot implementation. This similarity is further supported by a Root Mean Square Error (RMSE) of just 290 μm between pixel-wise thickness values extracted from the phase image obtained using the single-shot [Fig. 2(e)] and the sample dithering [Fig. 2(c)] methods, which has to be compared with a random background noise in the single shot thickness image of 260 μm. In general, an RMSE between single-shot and sample dithering methods within the former's average noise level was observed for samples composed of structures larger than the single-shot resolution. A more comprehensive study of the similarity between single-shot and sample dithering is provided in the supplementary material. The RMSE between thickness values extracted from phase and attenuation images was found to be 695 μm, which reflects the incorrect retrieval using either phase method observed in the left part of the beetle image in Figs. 2(c) and 2(e). The discrepancies are likely caused by the limited field of view, making differential phase integration incorrect. In addition, the differential phase signal may not be completely accurate despite the implemented corrections for problems caused by overlapping beamlets, low counting statistics, etc. Furthermore, beam hardening and coherent scattering distort the predicted thickness found from attenuation and phase signal in different ways, which can cause discrepancies between the two.

In Fig. 4, a silicon carbon fiber (Goodfellow SI675721) loop was used to test the directional ability of the scatter signal; according to the manufacturer, the individual fibers are 15 μm in diameter, and
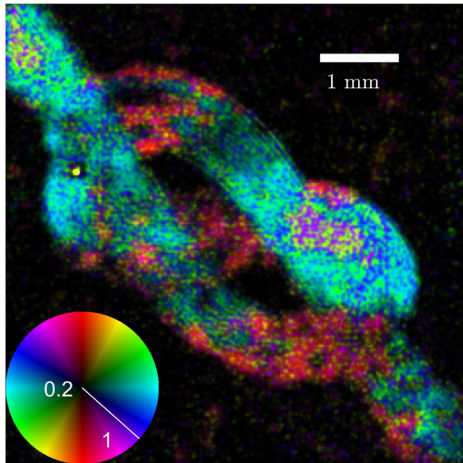
FIG. 4. Single-shot directional dark field image of a looped bundle of approximately 15-μm-thick silicon carbon fibers, with the scattering signal expressed through HSV (hue = orientation, brightness set constant; value = scattering strength in arbitrary normalized units) with the color scale as indicated by the color wheel.

therefore, similar to the beamlets' FWHM at the sample. The latter were are found to be 15 ± 2 μm thick, and this value determines the ultimate resolution of the imaging system.[32] All setup parameters are the same in this case as described in relation to Fig. 1. The strength of the scatter signal scales with the magnitude and orientation of the microscopic sample gradient and is, therefore, expected to be strongest orthogonal to the carbon wire orientation, as shown in Fig. 4, retrieved from a single-shot image. To mitigate the effect of imprecisions on the retrieval of beamlet variance and co-variance caused by overlapping beamlets, a mean filter was applied before calculating the orientation and magnitude of the primary scattering signal from the covariance matrix in Eq. (7).

In a previous paper,[22] we showed how the dark field signal is complementary to attenuation and differential phase signals by imaging a slice of bamboo wood, the hierarchical nature of which ensures the presence of features at multiple length scales. This has been repeated with the MÖNCH-based setup, and results are reported in the supplementary material (Fig. S4).

In summary, we have shown a range of preliminary results indicating that a setup based on the MÖNCH detector enables us to obtain reliable thickness maps and directional scatter images from single-shot images acquired without any movement of the mask and/or the sample, with resolution determined by the beamlet spacing at the sample (19.5 μm). In terms of resolution obtained for single-shot multimodal images, this is almost eight times smaller than 150 μm previously obtained using Timepix3.[19] We experienced problems with the accurate determination of the various image channels as a function of narrow energy bins, in particular at low energy, possibly caused by coherent scattering from the sample supports and fluorescence emission from the detector board (mainly copper), due to a non-negligible fraction of x-rays transmitted through the silicon sensor. The latter could be mitigated by using thicker silicon sensors or higher Z materials (e.g., GaAs).[33] The degree of overlap between beamlets, which imposed the use of a mean filter on the extraction of directional scatter images and affected our ability to retrieve quantitatively correct phase

values, could possibly be overcome by employing more sophisticated retrieval approaches.[34] Alternatively, reducing the mask apertures in combination with the use of a nano-focus source would decrease the width of the beamlets without significantly reducing the beamlets' intensity. The combination of a nano-focus source and the MÖNCH detector's high-resolution and high-sensitivity has already been demonstrated to be a good match.[28]

See the supplementary material for the details on the sub-pixel interpolation algorithm (Sec. S1), quantitative accurate retrieval of the sample thickness with the MÖNCH setup (Sec. S2), and RMSE calculation between single-shot and dithered phase images (Sec. S4). In Sec. S3, we illustrate the complementary of the image modalities accessible with our technique.

DATA AVAILABILITY

The data that support the findings of this study are available from the corresponding author upon reasonable request.

REFERENCES

[1]T. J. Davis, D. Gao, T. E. Gureyev, A. W. Stevenson, and S. W. Wilkins, Nature **373**, 595–598 (1995).

[2]F. Pfeiffer, M. Bech, O. Bunk, P. Kraft, E. F. Eikenberry, C. Brönnimann, C. Grünzweig, and C. David, Nat. Mat. **7**, 134 (2008).

[3]M. Bech, A. Tapfer, A. Velroyen, A. Yaroshenko, B. Pauwels, J. Hostens, P. Bruyndonckx, A. Sasov, and F. Pfeiffer, Sci. Rep. **3**, 3209 (2013).

[4]K. Hellbach, A. Baehr, F. De Marco, K. Willer, L. B. Gromann, J. Herzen, M. Dmochewitz, S. Auweter, A. A. Fingerle, P. Nöel, E. J. Rummeny, A. Yaroshenko, H.-I. Maack, T. Pralow, H. van der Heijden, N. Wieberneit, R. Proska, T. Koehler, K. Rindt, T. J. Schroeter, J. Mohr, F. Bamberg, B. Ertl-Wagner, F. Pfeiifer, and M. F. Reiser, Sci. Rep. **8**, 2602 (2018).

[5]L. B. Gromann, F. De Marco, K. Willer, P. Nöel, K. Scherer, B. Renger, K. Achterhold, A. A. Fingerle, D. Muenzel, S. Auweter, K. Hellbach, M. Reiser, J. Koch, P. Meyer, D. Kunka, J. Mohr, A. Yaroshenko, H.-I. Maack, T. Pralow, H. van der Heijden, R. Proska, T. Koehler, N. Wieberneit, K. Rindt, E. J. Rummeny, F. Pfeiffer, and J. Herzen, Sci. Rep. **7**, 4807 (2017).

[6]M. Endrizzi, P. C. Diemoz, T. P. Millard, J. L. Jones, R. D. Speller, I. K. Robinson, and A. Olivo, Appl. Phys. Lett. **104**, 024106 (2014).

[7]T. Rauch, J. Rieger, G. Pelzer, F. Horn, R. Erber, M. Wunderle, J. Emons, N. Nabieva, N. Fuhrich, T. Michel, A. Hartmann, P. A. Fasching, and G. Anton, Med. Phys. **47**, 1813 (2020).

[8]M. S. Nielsen, T. Lauridsen, L. B. Christensen, and R. Feidenhans'l, Food Control **30**, 531 (2013).

[9]V. Revol, I. Jerjen, C. Kottler, P. Schültz, R. Kaufmann, T. Lüthi, U. Sennhauser, U. Straumann, and C. Urban, J. Appl. Phys. **110**, 044912 (2011).

[10]M. Kagias, Z. Wang, M. E. Birkbak, E. Lauridsen, M. Abis, G. Lovric, K. Jefimovs, and M. Stampanoni, Nat. Commun. **10**, 5130 (2019).

[11]C. K. Hagen, P. Maghsoudlou, G. Totonelli, P. C. Diemoz, M. Endrizzi, L. Rigon, R.-H. Menk, F. Arfelli, D. Dreossi, E. Brun, P. Coan, A. Bravin, P. D. Coppi, and A. Olivo, Sci. Rep. **5**, 18156 (2015).

[12]P. Modregger, J. Meganck, C. K. Hagen, L. Massimi, A. Olivo, and M. Endrizzi, Phys. Med. Biol. **64**, 205008 (2019).

[13]A. Olivo and R. Speller, Appl. Phys. Lett. **91**, 074106 (2007).

[14]F. A. Vittoria, G. K. N. Kallon, D. Basta, P. C. Diemoz, I. K. Robinson, A. Olivo, and M. Endrizzi, Appl. Phys. Lett. **106**, 224102 (2015).

[15]H. H. Wen, E. E. Bennett, R. Kopace, A. F. Stein, and V. Pai, Opt. Lett. **35**, 1932 (2010).

[16]H. Wang, Y. Kashyap, and K. Sawhney, Sci. Rep. **6**, 20476 (2016).

[17]I. Zanette, T. Zhou, A. Burvall, U. Lundström, D. H. Larsson, M. Zdora, P. Thibault, F. Pfeiffer, and H. M. Hertz, Phys. Rev. Lett. **112**, 253903 (2014).

[18]E. S. Dreier, C. Silvestre, J. Kehres, D. Turecek, M. Khalil, J. H. Hemmingsen, O. Hansen, J. Jakubek, R. Feidenhans'l, and U. L. Olsen, J. Instrum. **14**, C01011 (2019).

[19]E. S. Dreier, C. Silvestre, J. Kehres, D. Turecek, M. Khalil, J. H. Hemmingsen, O. Hansen, J. Jakubek, R. Feidenhans'l, and U. L. Olsen, Opt. Lett. **45**, 1021 (2020).

[20]G. Sato, T. Kondoh, H. Itoh, S. Handa, K. Yamaguchi, T. Nakamura, K. Nagai, C. Ouchi, T. Teshima, Y. Setomoto, and T. Den, Opt. Lett. **36**, 3551 (2011).

[21]K. S. Morgan, D. M. Paganin, and K. K. W. Siu, Opt. Exp. **19**, 19781 (2011).

[22]F. A. Vittoria, M. Endrizzi, P. C. Diemoz, U. H. Wagner, C. Rau, I. K. Robinson, and A. Olivo, Appl. Phys. Lett. **104**, 134102 (2014).

[23]K. R. Rix, T. Dreier, T. Shen, and M. Bech, "Super-resolution x-ray phase-contrast and dark-field imaging with a single 2D grating and electromagnetic source stepping," Phys. Med. Biol. **64**, 165009 (2019).

[24]M. Ramilli, A. Bergamaschi, M. Andrae, M. Brückner, S. Cartier, R. Dinapoli, E. Fröjdh, D. Greiffenberg, T. Hutwelker, C. Lopez-Cuenca, D. Mezza, A. Mozzanica, M. Ruat, S. Redford, B. Schmitt, X. Shi, G. Tinti, and J. Zhang, J. Instrum. **12**, C01071 (2017).

[25]S. Cartier, M. Kagias, A. Bergamaschi, Z. Wang, R. Dinapoli, A. Mozzanica, M. Ramilli, B. Schmitt, M. Brückner, E. Fröjdh, D. Greiffenberg, D. Mayilyan, D. Mezza, S. Redford, C. Ruder, L. Schädler, X. Shi, D. Thattil, G. Tinti, J. Zhang, and M. Stampanoni, J. Synchrotron Rad. **23**(6), 1462–1473 (2016).

[26]M. Khalil, E. S. Dreier, J. Kehres, J. Jakubek, and U. L. Olsen, J. Synchrotron Rad. **25**, 1650 (2018).

[27]C. Dullin, J. Albers, G. Tromba, M. Andrä, M. Ramilli, and A. Bergamaschi, J. Synchrotron Rad. **25**, 565 (2018).

[28]L. M. Lohse, M. Vassholz, M. Töpperwien, T. Jentschke, A. Bergamaschi, S. Chiriotti, and T. Salditt, Opt. Exp. **28**, 9842 (2020).

[29]P. Modregger, M. Kagias, S. C. Irvine, R. Brönnimann, K. Jefimovs, M. Endrizzi, and A. Olivo, Phys. Rev. Lett. **118**, 265501 (2017).

[30]G. K. Kallon, M. Wesolowski, F. A. Vittoria, M. Endrizzi, D. Basta, T. P. Millard, P. C. Diemoz, and A. Olivo, Appl. Phys. Lett. **107**, 204105 (2015).

[31]S. Kühsel, A. Brückner, S. Schmelzle, M. Heethoff, and N. Blüthgen, Insect Sci. **24**, 829 (2017).

[32]P. C. Diemoz, F. A. Vittoria, and A. Olivo, Opt. Exp. **22**, 15514 (2014).

[33]J. Scholz, L. Birnbacher, C. Petrich, M. Riedel, L. Heck, S. Gkoumas, T. Sellerer, K. Achterhold, and J. Herzen, APL Photonics **5**, 106108 (2020).

[34]C. J. Maughan Jones, F. A. Vittoria, A. Olivo, M. Endrizzi, and P. R. T. Munro, Opt. Lett. **43**, 3874 (2018).